Quantitative Organ Visualization Using SPECT

Louis T. Kircos, James E. Carey, Jr., and John W. Keyes, Jr.

Department of Radiology, University of California, San Francisco, California; Division of Nuclear Medicine, University of Michigan Medical Center, Ann Arbor, Michigan; and Department of Radiology, Georgetown University, Washington, DC

Quantitative organ visualization (QOV) was performed using single photon emission computed tomography (SPECT). Organ size was calculated from serial, contiguous ECT images taken through the organ of interest with image boundaries determined using a maximum directional gradient edge finding technique. Organ activity was calculated using ECT counts bounded by the directional gradient, imaging system efficiency, and imaging time. The technique used to perform QOV was evaluated using phantom studies, in vivo canine liver, spleen, bladder, and kidney studies, and in vivo human bladder studies. It was demonstrated that absolute organ activity and organ size could be determined with this system and total imaging time restricted to <45 min to an accuracy of about ±10% providing (a) the minimum dimensions of the organ are > the FWHM of the imaging system and (b) the total radioactivity within the organ of interest exceeds 15 nCi/cc for dog-sized torsos. In addition, effective half-lives of ~1.5 hr or greater could be determined.

J Nucl Med 28:334–341, 1987

At the 1970 conference on "Quantitative Organ Visualization in Nuclear Medicine," P.J. Kenny defined quantitative organ visualization (QOV) as " . . . knowledge of the absolute amount of activity in each volume element in the organ of interest in successive time intervals . . . " (*1*). He noted that at that time the capability to determine radionuclide distributions in three dimensions did not exist. Since then, with the development of techniques for single photon emission computed tomography (SPECT), the technology for accomplishing QOV, as Kenny defined it, has become available.

SPECT appears ideally suited for QOV. The tomographic approach permits the separation of structures which are superimposed in conventional images. This separation is further enhanced by the intrinsic high contrast of SPECT images. The reconstruction of contiguous, thin sections permits evaluation of the three-dimensional distribution of radioactivity and, when appropriate corrections are made for attenuation losses, the SPECT images can allow quantification of organ size, shape, and radioactivity.

Several authors have utilized these characteristics to quantitate both phantom and in vivo radioactivity distributions using SPECT (*2–6*) and positron emission computed tomography (*7–12*). This paper is a report of our efforts to develop a technique for QOV, based upon a SPECT system, the Humongotron (*13*). We present techniques for quantifying organ volumes and the absolute amount of radioactivity within organs. In addition, an analysis of the accuracy of these methods is presented.

Received Nov. 5, 1985; revision accepted July 17, 1986.

For reprints contact: Louis T. Kircos, DDS, MS, PhD, Div. of Oral Radiology, University of California, San Francisco, San Francisco, CA 94143.

MATERIALS AND METHODS

All studies were performed using the Humongotron, a single photon emission computed tomography (ECT) system which has been previously described (*13*). This system, which incorporates a Searle® Pho/Gamma III HP scintillation camera, was used with either a Searle High Resolution collimator or a tantalum collimator specially designed for tomography at technetium-99m (^{99m}Tc) energies (*14*). The images were digitized and stored on disk using a commercially available nuclear medicine computer system,† which was also used for image reconstruction. A convolution-type reconstruction algorithm was employed with a filter function similar to Budinger's "new filter" (*15,16*). Attenuation correction was performed using the "mean exponential technique" of Kay (*17*) assuming elipsoidal body margins and a uniform attenuation coefficient of u = 0.15/cm.

Serial, contiguous SPECT images of selected organ(s) of

interest were analyzed by the technique described by Kircos (*16,18*). This technique assumes an isotropic tomographic imaging system response function and is based upon computing a five point, least squares, directionally sensitive first derivative (LSDSFD) of the image which results in a deconvolution of the imaging system response function from the object. The processed image shows each organ edge outlined in a topographic manner representative of the gradients of the original image. A profile normal to the organ edge is the system response function (Fig. 1) for organ edges which can be considered step functions in the tomographic plane. The geometric edge of the organ is defined by the maximum of this deconvolved imaging system response function. It has been shown (*16,18*) that this technique is mathematically exact for sources of radioactivity whose exposed edges can be considered either a step or a ramp function in the tomographic plane (Fig. 1). Once the edge had been established, the size of the organ of interest was determined by measuring the area (in square pixels) encompassed by the edge of the organ of interest (A_k), summing over all the tomographic sections containing the organ (k), multiplying by pixel size (P_x^2), section thickness (DeltaZ), and tissue density (rho) (*19*):

$$M(gm) = (rho)(DeltaZ)(P_x^2) \sum_{k=1}^{k} (A_k), \quad (1)$$

where k is the number of tomographic sections through which the organ of interest extends in the third dimension. The extent of the integration in the third dimension is established by the observation of the point near the periphery of the organ where the counts per pixel fall to about 50% of the value observed at a slightly more central location (Fig. 1A).

The absolute quantity of radioactivity in the organ of interest (Q) also was determined by analysis of the deconvolved imaging system response function (Fig. 1). Blurring introduced by the imaging system tends to spread organ counts beyond its geometric boundaries in the SPECT image causing difficulty in determining the radioactivity in the organ of interest. To correct for this, the number of counts (N_k) were determined within an area (a_k) which extends beyond the geometric border of the organ (Figs. 1 and 2) and encompasses the full extent of the deconvolved imaging system response function (Figs. 1A and 2D). This was accomplished by flagging this extended area manually with a light pen in the first derivative image (Fig. 2B) and then determining the number of counts within the same area in the original SPECT image. The integration in the third dimension is extended until the counts per pixel falls to ~10% of the value observed in a slightly more central location. Organs distributed in a uniform media of radioactivity also required background subtraction:

$$N_k' = N_k - (n)(a_k), \quad (2)$$

where n is equal to the background intensity in counts per pixel squared. This, together with the factors for imaging system efficiency (E) and imaging time (Delta t), are sufficient to determine the absolute quantity of radioactivity in the organ of interest.

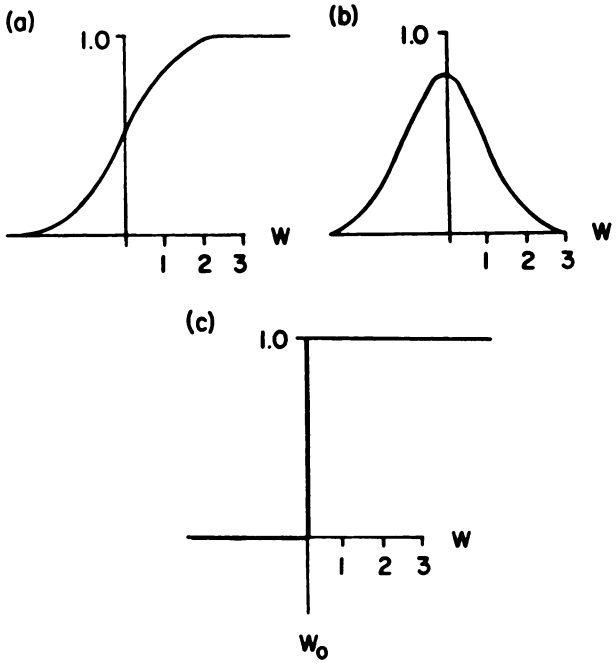

FIGURE 1
Technique for defining organ edges and extent of radioactivity: (A) Profile through a "perfect organ edge" which is a convolution of the PSF (B) with an organ edge represented by a step function (C). The organ edge (C) is defined by the maximum of (B) which is the first derivative of (A). The number of counts attributable to the organ extend beyond the geometric edge (C) and is outlined by the extent of the gradient (B).

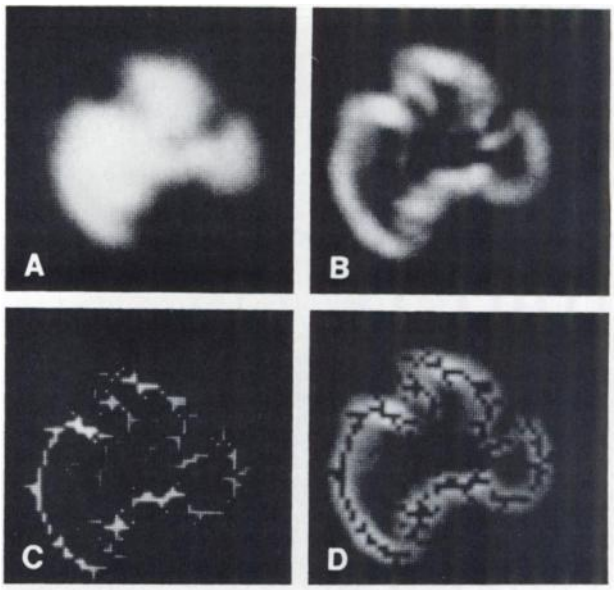

FIGURE 2
Technique for defining organ edges and extent of organ radioactivity, clinical example. A: Tomographic section of dog liver. B: Directionally sensitive first derivative (gradient) of tomogram in A. The extent of the gradient determines the area over which counts are integrated for activity determinations. C: Maximum of the first derivative (gradient) image, B. This outline defines the geometric border of the organ and was used to determine organ size. D: Organ border superimposed on the first derivative image. Note how the gradient extends beyond the organ border and defines the extent of counts attributable to the radioactivity in the liver.

$$Q(uCi) = (E)/(Delta\ t) \sum_{k=1}^{k} N_k'. \quad (3)$$

From this equation, the absolute mean concentration of radioactivity in the organ can be found by dividing by the calculated mass of the organ (Eq. 1) and multiplying by the density. The system efficiency, E, is defined as the reciprocal of counts per mCi second and empirically derived from regression analysis of Figure 9.

Phantom and Clinical Studies

A variety of phantom and animal studies were performed to evaluate these techniques. The choice of studies was based on the objective of providing relatively inclusive coverage of the imaging situations that might be encountered in performing QOV. Technetium-99m in various chemical forms was used in most studies with the exception of thallium-201 (^{201}Tl) which was used for the kidney studies. Imaging times varied from 10 to 45 min.

The phantoms included a cylindrical absorption phantom 17.2 cm in diameter in which focal volumes of radioactivity could be placed in a radioactive or nonradioactive milieu (Fig. 3)—a resolution bar phantom consisting of various slots milled in a block of lucite which could be filled with radioactive fluid (Fig. 4); a 15.0 cm diameter cylindrical polystyrene quality control phantom in which line sources of radioactivity could be accurately placed (*14*); and an anatomic phantom, ELRAD (Figs. 5 and 6), which consists of a hollow plastic torso in which a variety of hollow, simulated organs can be placed containing varying amounts of radioactivity.

In vivo studies were performed on mongrel dogs ranging in weight from 14.0 kg to 25.0 kg. Liver and spleen studies were performed using [^{99m}Tc]sulfur colloid, bladder studies with [^{99m}Tc]pertechnetate or pyrophosphate, and a kidney study with ^{201}Tl. The dogs were anesthetized with sodium pentobarbital, scanned, killed, and the organs of interest were removed. For bladder studies, the urine was removed from the bladder, measured volumetrically, then assayed in a Capintec CRC 2N ionization chamber dose calibrator.‡ For liver-spleen studies, tissue samples for the organ of interest were removed, weighed, and counted in a Packard 5320 well-type scintillation counter.§

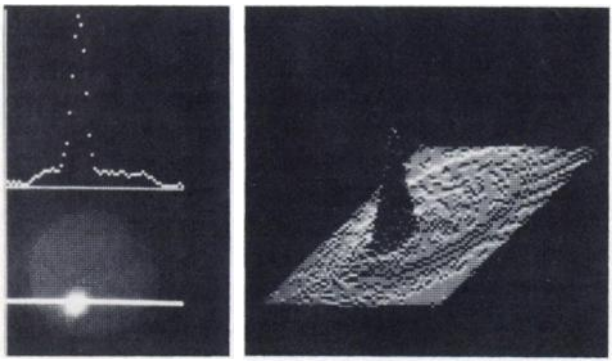

FIGURE 3
Absorption phantom. This is a SPECT image of the absorption phantom with the large compartment and one tube filled with low and high concentrations of activity respectively. This phantom is 17.2 cm in diameter and 25 cm long. It has a volume of 5,800 cm^3. Different imaging situations are produced by the inclusion of up to three 19 mm diameter tubes located on a 4.5 cm radius from the center of the phantom.

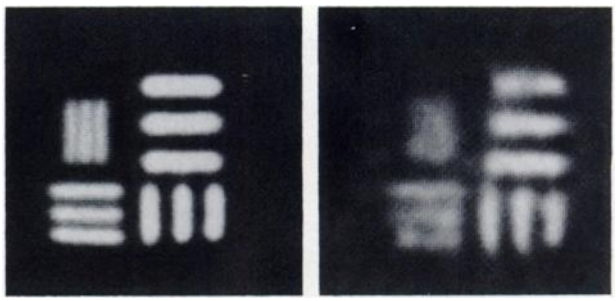

FIGURE 4
Resolution phantom. The image on the left is a planar image of the resolution phantom obtained by placing the phantom in contact with the collimator face. The image on the right is a SPECT of the same phantom. This phantom is made of lucite and has slots milled in it in which various quantities of radioactivity can be placed and measures 15 × 15 × 5.1 cm thick. The slots measure 6.5 × 1.6; 5.0 × 1.3; 6.0 × 1.0; and 6.0 × 0.7 cm, respectively.

In addition, a calibration curve was obtained ($r^2 > 0.99$) for each study by counting a number of serial dilutions of a known amount of [^{99m}Tc]pertechnetate in the scintillation counter. From this calibration curve the absolute concentration of radioactivity in μCi/g was computed for the organ of interest. The weight of the organ of interest was recorded.

RESULTS

Representative phantom data are presented in Table 1 and illustrated in Figure 7. Data to determine the accuracy of this technique for half-life measurements are presented in Figure 8. These time lapse studies include data obtained from the absorption phantom filled with a uniform distribution of radioactivity (Curve 1, Fig. 8) and also the same phantom containing a focal source of radioactivity (Curve 2, Fig. 8) within a more dilute uniform distribution of activity (Curve 3, Fig. 8).

The in vivo results (Table 2) substantiate the accuracy of the technique as demonstrated in the phantom studies (Table 1) with the exception of the spleen data. This error results from a technical problem due to the rapid loss of splenic blood volume following killing and before the spleen could be removed and weighed.

In addition to the phantom and canine studies, an in vivo human bladder study was performed using [^{99m}Tc] pyrophosphate. Although the Humongotron is not well suited to studies of the human torso because of its limited field-of-view, the actual voided urine volume of 250 cc with a radioactivity of 950 μCi compared reasonably well with the computed volume of 299 cc and activity of 1,010 μCi. The difference may be a reflection of the technical conduct of the study including limited field-of-view, nonideal attenuation correction, etc., or patient management, i.e., residual urine or movement during the study.

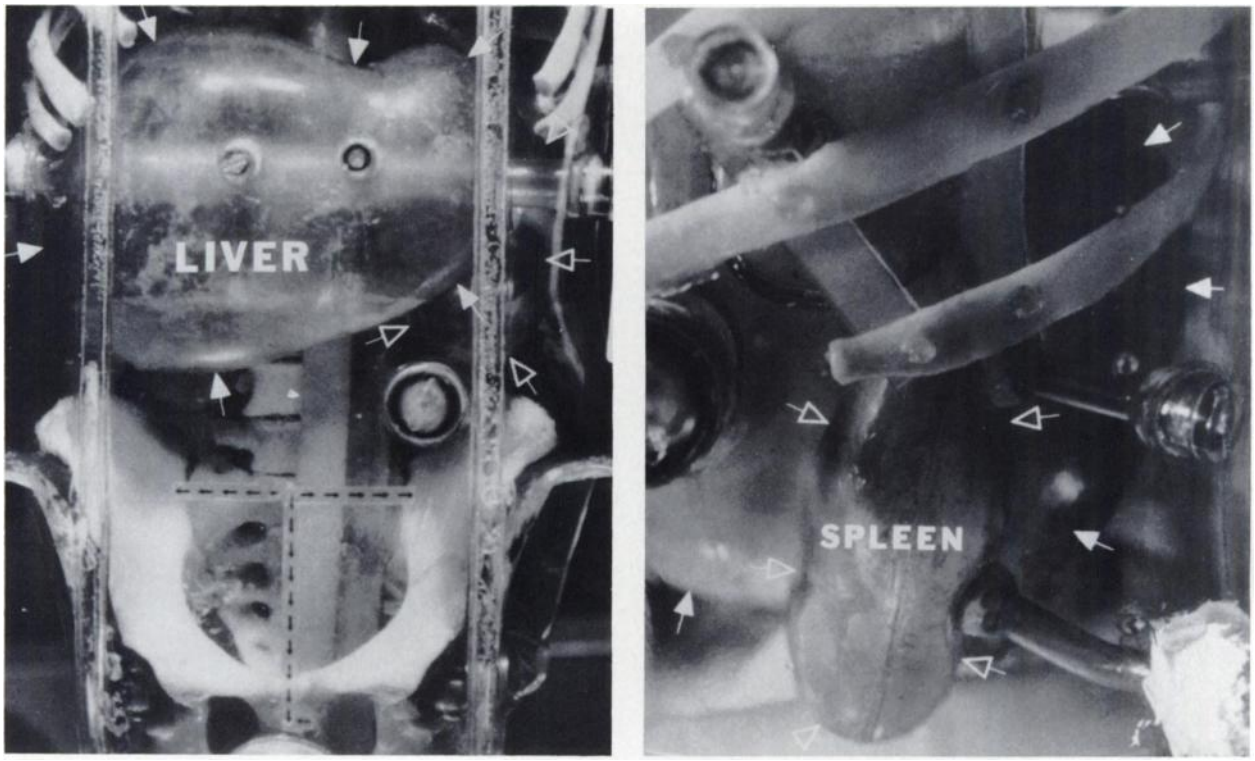

FIGURE 5
ELRAD. The picture on the left is an anterior view demonstrating the liver in solid arrows and the spleen in hollow arrows. The picture on the right is a left lateral view. Note on these views the close resemblance of human anatomy and the actual inclusion of a human skeleton.

The lower limit to the usefulness of this technique for organ sizing appears to be limited by the resolution of the imaging system (Fig. 9). A Gaussian spread function with a full width half maximum (FWHM) of 16.0 mm (approximately equal to the response function of the Humongotron in these studies) was convolved with rectangular step functions of various widths. The resulting functions were sized by the derivative technique already described and the results plotted. The curve is linear down to approximately the FWHM value of 16.0 cm, below which it rapidly flattens out and no objective size information can be obtained. Also shown in Figure 9 are data points from measurements obtained on phantoms which correspond to the theoretical predictions.

DISCUSSION

The phantom and canine studies produced QOV results which agree relatively closely with measured organ size and activity concentration, with the exception of the spleen data as already noted. These results indicate that, with the techniques described, it is possible to determine the size and absolute quantity of

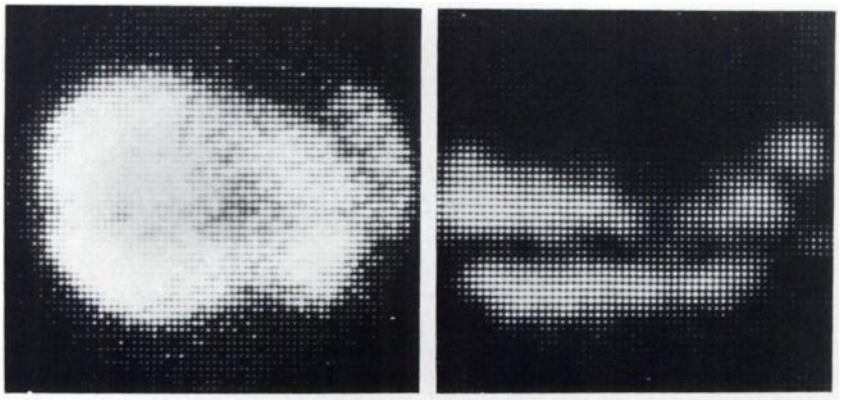

FIGURE 6
The image at left is an AP planar image of ELRAD's liver and spleen. The image at right is a SPECT image through the bottom third of ELRAD's liver demonstrating a 1-in. tub located in the liver which was not filled with activity. The inferior tip of ELRAD's spleen can be appreciated in the SPECT image in the posterior right, adjacent to the liver.

TABLE 1
Phantom Studies

Phantom	Location	Actual activity (μCi)	Computed activity (μCi)	Actual volume (cc)	Computed volume (cc)	Size error (%)	Activity error (%)
1. ELRAD	Liver	780.0	750.0	1,280.0	1,247.0	3	3
2. ELRAD	Spleen	63.0	65.0	105.0	96.0	8	12
3. ELRAD	Bladder	42.8	40.5	4.30	4.90	14	5
4. ELRAD	Bladder	39.4	38.5	4.30	4.90	14	2
5. Absorption	Tube 1	3.32	3.96	2.17	1.93	11	19
6. Absorption	Tube 2	2.02	2.31	2.17	1.91	11	14
7. Absorption	Tube 3	1.02	*	2.17	*	*	*
8. Absorption	Volume	54.4	56.9	176.0	184.0	1	5
9. Absorption	Tube 1	51.0	54.4	2.17	2.05	5	7
10. Absorption	Tube 2	28.3	31.5	2.17	2.00	8	11
11. Absorption	Volume	120.0	127.0	176.0	178.0	1	6
12. Resolution	Small bars	56.0	60.0	3.4	*	*	7
13. Resolution	Medium bars	62.0	67.0	3.8	4.6	17	8
14. Resolution	Big bars	96.0	104.0	5.8	6.5	13	8
15. QC	Line source	98.0	100.0	<0.1	*	*	2

* Cannot resolve.

radioactivity in organs to an accuracy of ~±10% for relatively small uniformly distributed sources. The radioactivity determination is dependent on a number of factors including linearity of the imaging and reconstruction processes as well as an accurate technique for attenuation compensation (*20–31*). The techniques employed here worked well for dog-size torsos and uniform attenuators. Presumably, these errors would increase for larger, human torsos.

Unexpectedly, however, the human phantom studies using ELRAD and the sole in vivo bladder study produced relatively accurate estimations of the activity and the size of the radioactive source. In these cases, the theoretical tendency of the attenuation compensation routine to underestimate N_k for large objects may have

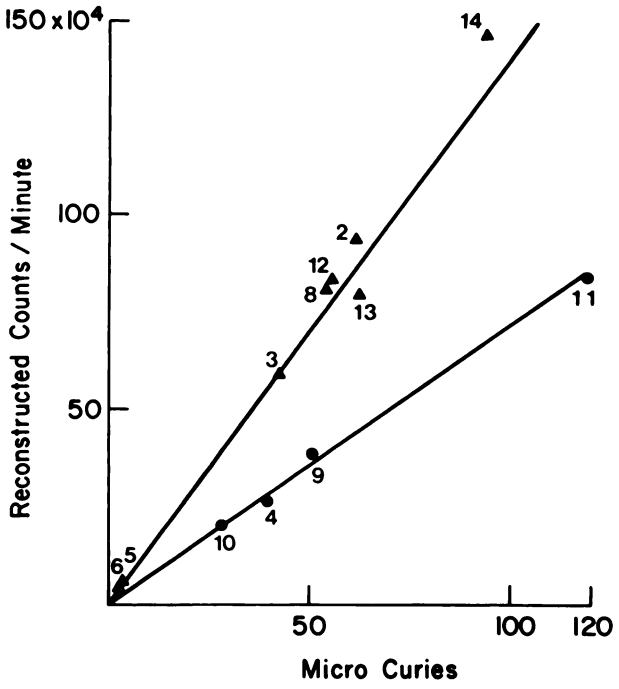

FIGURE 7
Relationship between the total counts in the reconstructed images to the actual radioactivity in the various phantom studies, i.e., calibration curves. The different slopes of these two curves reflect the different sensitivities of the high resolution and the specially designed tantalum collimator. (●) TOMO collimator; (▲) Searle HR collimator.

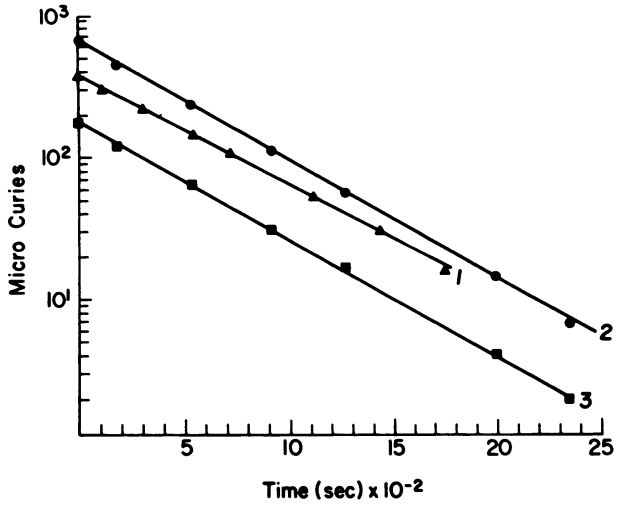

FIGURE 8
Calculated radioactivities in various geometries of the absorption phantom (Fig. 3) versus time. These curves were used to evaluate the usefullness of these techniques for half life measurements and give a measure of the limit detectability of this SPECT system and these techniques.

TABLE 2
In Vivo Studies

Subject (kg)	Organ	Actual size	Computed size	Error (%)	Actual activity	Computed activity	Error (%)
Human (80) k	Bladder	250 cc	299 cc	20	3.80 μCi/cc	3.41 μCi/cc	10
Dog (20) k	Liver	628 g	651 g	4	9.33 μCi/g	8.60 μCi/g	8
Dog (25) k	Liver	874 g	942 g	8	4.33 μCi/g	3.90 μCi/g	10
Dog (16) k	Liver	632 g	640 g	3	3.90 μCi/g	2.93 μCi/g	5
Dog (16) k	Spleen	61 g	137 g	*	13.2 μCi/g	6.86 μCi/g	*
Dog (25) k	Spleen	127 g	317 g	*	4.15 μCi/g	3.81 μCi/g	*
Dog (20) k	Bladder	260 cc	258 cc	1	3.96 μCi/cc	3.81 μCi/cc	4
Dog (16) k	Bladder	116 cc	110 cc	6	47.7 μCi/cc	44.8 μCi/cc	5
Dog (25) k	Bladder	290 cc	303 cc	4	6.48 μCi/cc	6.44 μCi/cc	1
Dog (18) k	Kidney	106 g	107 g	1	1.82 μCi/g	1.63 μCi/g	10

* Splenic volumes show large apparent error due to postmortem decrease in spleen volume that occurred before the organ could be removed and weighed.

been partially compensated for by an increase in N_k due to Compton scatter (*23,24,28*). Although the use of a uniform attenuation coefficient for the dog studies and the study of ELRAD's liver appears reasonable, the use of a uniform attenuation coefficient for ELRAD's bladder and the human bladder study is somewhat questionable because of the increase in attenuation from portions of the pelvis and the coccyx/sacrum. However, for this limited study the results are satisfactory and CT of the lower pelvis indicates the volume of bone attenuating the photons may be reasonably small in comparison to the volume of soft tissue and may not cause the major errors in quantification that would seem apparent from casual consideration.

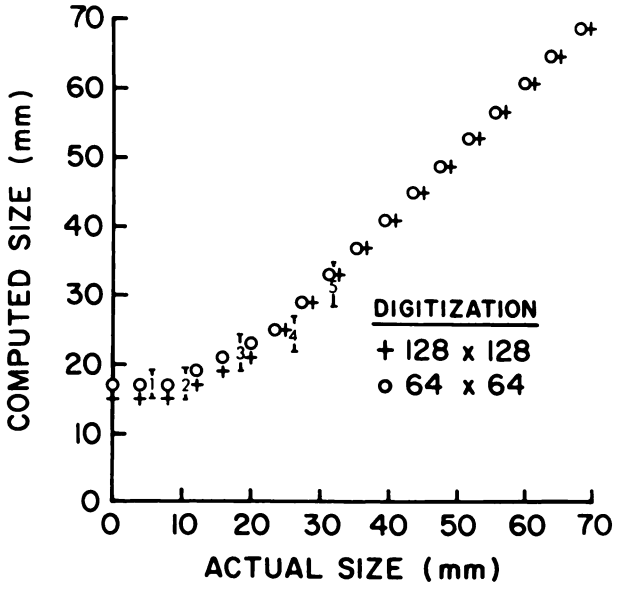

FIGURE 9
Relationship between actual size and computed size for computer generated data. The derivative techniques described here were used to size various width steps and plotted for two levels of matrix digitization, 64 and 128. The numbers 1 through 5 appearing between the curves are actual phantom measurements using the imaging system and techniques described here.

The time lapse studies introduce the possibility of determining effective half-lives in vivo. The physical half-life of ^{99m}Tc, as determined from the slope of the curves shown in Figure 8, is within 0.5% of its known value with $r^2 > 0.99$. Assuming a 20-min scan time and a 10% error in the determination of the absolute concentration of radioactivity, effective half-life determination of ~1.5 hr are possible. For effective half-lives <1.5 hr, the error in the estimation becomes greater.

Figure 9 shows that there is a systematic overestimation of organ dimensions which are less than the FWHM of the imaging system and that, below FWHM/2, no useful size information can be obtained. Figure 9 also shows that there can be size determination errors of about half a pixel even for perfect data. Thus, providing a smaller image matrix slightly improves the accuracy of size determinations, especially for small organs. Organs whose minimum dimension in any direction is smaller than the FWHM of the imaging system cannot be accurately sized without the knowledge of the absolute concentration of radioactivity in the organ of interest. When the absolute radioactivity and concentration of radioactivity within the organ of interest are known, the volume of the organ is simply the activity divided by the concentration of radioactivity. Many organ sizing techniques, especially thresholding, rely on a predictable concentration of radioactivity in the organ of interest for accurate results (*3,5,32*). Note, however, that accurate quantification of the amount of radioactivity in the organ still can be obtained, independent of size.

The limit of detection of these techniques was established with studies of the absorption phantom (Table 2 and Fig. 8). The limit of detection is dependent on the geometry and intensity of the sources in the tomographic plane (and near planes) as well as the geometry of attenuators in the tomographic plane. There is diffi-

culty in generalizing the results of these studies because of the infinite variability of the size, shape, intensity, and relative location of sources and attenuators encountered in clinical imaging situations, all of which have an effect on their ultimate detectability. However, studies of the absorption phantom indicate that, for this geometry, an absolute radioactivity of about 5.5 μCi (15 nCi/cc for the large compartment, uniform distribution) and about 1 μCi (250 nCi/cc) for the tubular insert (focal area) in the absorption phantom produce SPECT images close to the lower limit of detectability by these techniques. These results were dependent on the duration of the study and the geometry of the attenuator, and they reflect a 40-min study time and attenuators of about the size of a dog's torso. In general, the detectability of multiple sources is dependent on their location, size and shape, absolute and relative concentration of radioactivity, geometry and size of attenuator, and the duration of the study. These are only samples of a complex imaging problem and represent an area where further study should be directed for resolution.

In general, the accuracy of the techniques employed are limited by the characteristics of the imaging system. The volume determinations are limited by the FWHM, image matrix size, noise, and the assumption of a linear and isotropic imaging system. Radioactivity determinations are limited by attenuation correction, noise, and related factors including scatter, uniformity, energy window, etc. (*20–31*), and are independent of the volume determinations.

Although the sensitivity of this technique is less than that obtained by counting tissue samples in a well-type scintillation counter (which often produces errors >±10%), it does introduce the possibility of human dosimetry using in vivo human data. Using this technique, human data on organ size, radionuclide concentration, and effective half-life could be obtained.

Currently, radiopharmaceuticals are assessed and dose calculations performed on the basis of animal studies (*33–36*). The major difficulty in performing Medical Internal Radiation Dose Committee dosimetry is the determination of A, the accumulated activity which is based on the knowledge of the time course of radioactivity in the organ of interest (*37*). This is now done by performing tissue distribution studies of the radiopharmaceutical of interest in animals and extrapolating the data to humans. The basis of extrapolation of animal data to humans is equivocal (*38–40*) and the reliability of dosage calculations based on such data may be in error of up to an order of magnitude (*41*). Potentially, QOV can determine the parameters associated with radiopharmaceuticals in vivo such as uptake (kg % dose/g, target to nontarget ratio (T/NT), and the biologic half-life in humans. There is a current need for measurements of these parameters in normal patients, in pediatric patients, and in patients with altered physiology and anatomy (*42*). Dosage calculations are inherently more accurate when based on radiopharmaceutical parameters determined in vivo in man because the behavior of a radiopharmaceutical in vivo is the reflection of human anatomy and physiology which no animal can suitably mimic.

The results are based on a Searle Pho Gamma III HP, a relatively old camera. Although newer cameras have increased intrinsic resolution, this would not translate into dramatic increases in overall resolution for SPECT systems. The resolution of SPECT systems is dominated by the characteristics of the collimator and the radius of rotation so that improvements in intrinsic resolution have only a minor effect on SPECT resolution (*14*). However, preprocessing appears to provide small improvements in resolution (*43–44*) and improvements in camera uniformity and uniformity corrections appear to provide some improvement in quantitation (*27–31*).

Although the results demonstrated are for a specific SPECT system, they should apply to most SPECT systems, providing that the requirements for accurate attenuation correction and for a linear, isotropic imaging system are met. Since the sensitivity and resolution of our present system are representative of most SPECT systems currently available it appears that ECT techniques will permit the accomplishment of QOV within useful limits.

NOTES

* Siemens Medical Systems, Islen, NJ.
† Medical Data Systems, Ann Arbor, MI (MDS "Trinary").
‡ Capintec, Inc., Ramsey, NJ.
§ Packard Instrument Co., Downers Grove, IL.

REFERENCES

1. Kenny PJ. What is quantitative organ visualization in nuclear medicine? In: Kenny PJ, Smith EM, eds. Quantitative organ visualization in nuclear medicine. Coral Gables, FL: University of Miami Press, 1971:1–13.
2. Kuhl DE, Edwards RQ, Ricci AR, et al. The Mark IV system for radionuclide computed tomography of the brain. *Radiology* 1976; 121:405–413.
3. Tauxe WN, Soussaline F, Todd-Pokropek A, et al. Determination of organ volume by single-photon emission tomography. *J Nucl Med* 1982; 23:984–986.
4. Macey DJ, DeNardo GL, Denardo SJ, et al. A calibration phantom for absolute quantitation of radionuclide uptake by SPECT [Abstract]. *J Nucl Med* 1984; 25:P105.
5. Malko JA, Eisner RL, Engdahl JC, et al. A threshold method of volume determination from tomographic reconstructions [Abstract]. *J Nucl Med* 1983; 24:P19.
6. Caldwell JH, Williams DL, Hamilton GW, et al. Regional distribution of myocardial blood flow measured by single-photon emission tomography: comparison with in vitro counting. *J Nucl Med* 1982; 23:490–495.
7. Brownell GL, Burnham CA, Chesler DA, et al. Trans-

verse section imaging of radionuclide distributions in heart, lung and brain. In: Ter-Pogossian MM, Phelps ME, Brownell GL, et al., eds. Reconstruction tomography in diagnostic radiology and nuclear medicine. Baltimore: University Park Press, 1977:293–307.
8. Phelps ME, Hoffman EJ, Huang S, et al. ECAT: a new computerized tomographic imaging system for positron-emitting radiopharmaceuticals. *J Nucl Med* 1978; 19:635–647.
9. Kuhl DE, Phelps ME, Hoffman EJ, et al. Initial clinical experience with (18)F-2-deoxy-D-glucose for determination of local cerebral glucose utilization by emission computed tomography. In: Ingvar DH, Lassen NA, eds. Cerebral function, metabolism and circulation. Copenhagen: Munksgaard, 1977:192–193.
10. Weiss ES, Ahmed SA, Welch MJ, et al. Quantification of infarction in cross sections of canine myocardium in vivo with positron emission transaxial tomography and (11)C-palmitate. *Circulation* 1977; 55:66–73.
11. Budinger TF, Derenzo SE, Huesman RH, et al. Role of tomography in providing radionuclide distribution and kinetic data. *Int J Nuc Med* 1983; 10:39.
12. Hoffman EJ, Huang SC, Phelps ME. Quantitation in positron emission computed tomography: I. Effect of object size. *J Comput Assist Tomogr* 1979; 3:299–308.
13. Keyes JW Jr, Orlandea N, Heetderks WJ, et al. The Humongotron—a scintillation camera transaxial tomography. *J Nucl Med* 1977; 18:381–387.
14. Kircos LT, Leonard PF, Keyes JW Jr. An optimized collimator for single photon computed tomography with a scintillation camera. *J Nucl Med* 1978; 19:322–323.
15. Budinger TF, Gullberg GT. Transverse section reconstruction of gamma-ray emitting radionuclides in patients. In: Ter-Pogossian MM, Phelps ME, Brownell GL, et al., eds. Reconstruction tomography in diagnostic radiology and nuclear medicine. Baltimore: University Park Press, 1977:315–342.
16. Kircos LT. Quantitative organ visualization. [Dissertation]. University of Michigan, 1978.
17. Kay DB, Keyes JW Jr. First order corrections for absorption and resolution compensation in radionuclide Fourier tomography. *J Nucl Med* 1975; 16:540–541.
18. Kircos LT, Keyes JW Jr, Carey JE. Edge finding techniques in emission computed tomography. *Med Phys* 1978; 5:352.
19. Geise R, McCullough E. The use of CT scanners in megavoltage photon-beam therapy planning. *Radiology* 1977; 124:133.
20. Walters TE, Simon W, Chesler DA, et al. Attenuation correction in gamma emission computed tomography. *J Comput Assist Tomogr* 1981; 5:89–94.
21. Gullberg GT, Budinger TF. The use of filtering methods to compensate for constant attenuation in single-photon emission computed tomography. *IEEE Transactions on Biomedical Engineering* 1981; BME-28(2):142–157.
22. Lewis MH, Willerson JT, Lewis SE, et al. Attenuation compensation in single-photon emission tomography: a comparative evaluation. *J Nucl Med* 1982; 23:1121–1127.
23. Oppenheim BE. Scatter correction for SPECT. *J Nucl Med* 1984; 25:928–929.
24. Jaszczak RJ, Greer KL, Gloyd CE, et al. Improved SPECT quantitation using compensation for scattered photons. *J Nucl Med* 1984; 25:893–900.
25. Siegal JA. The buildup factor: a general scheme for attenuation correction [Abstract]. *J Nucl Med* 1985; 26:P54.
26. Harris CC, Greer KL, Floyd CE, et al. Attenuation coefficients for Tc-99m photons in water-filled phantoms, determined with gamma camera: variation with window energy [Abstract]. *J Nucl Med* 1984; 25:P22.
27. Graham LS, LaFontaine RL, Stein MA. Effects of asymmetric photopeak windows on flood uniformity and spatial resolution of scintillation cameras. *J Nucl Med* 1986; 27:706–713.
28. Mukai T, Torizuka K, Douglas KH, et al. Improvement in quantitation in SPECT: attenuation and scatter correction using non-uniform attenuation data [Abstract]. *J Nucl Med* 1985; 26:P91.
29. Bixais YJ, Rowe RW, Zubal IG, et al. Linearity and energy corrections for scintillation cameras used in quantitative single photon emission computed tomography [Abstract]. *J Nucl Med* 1984; 25:P87.
30. Gregory RD, Savala J, Zendrt M, et al. Assessment of detector sensitivity and uniformity during SPECT rotation [Abstract]. *J Nucl Med* 1984; 25:P103.
31. Rogers WL, Clinthorne NH, Koral KF, et al. Field uniformity considerations for rotating gamma camera ECT [Abstract]. *J Nucl Med* 1981; 22:P21.
32. Keyes JW, Leonard PF, Brody SL, et al. Myocardial infarct quantification in the dog by single photon emission computed tomography. *Circulation* 1978; 58:227–232.
33. Richter CW, Anderson DW. In vivo dosimetry of (99m)Tc lung scanning agent. *Phys Med Biol* 1974; 19:73–78.
34. Jung A, Russell RGG, Bisag SP. Fate of intravenously injected pyrophosphate (32)p in dogs. *Am J Physiol* 1970; 218:1757–1764.
35. IAEA. Measurement of radioactivity in body organs. *Int J Appl Radiat Isotopes* 1971; 22:385–398.
36. Stevenson JS et al. The toxicity of Sn pyrophosphate: clinical manifestations prior to acute (LD)50. *J Nucl Med* 1974; 15:252–256.
37. Johnston RE. Internal dosimetry I. In: The physics of clinical nuclear medicine. AAPM Annual Summer School, Lexington: University of Kentucky, July 23–29, 1977:273–280.
38. Smith EM, Brownell GL, Ellett WH. Principles of nuclear medicine. In: Wagner HN Jr, ed. Radiation dosimetry. Philadelphia: WB Saunders, 1968:742.
39. Blau M. Radiation dosimetry of (131)iodocholesterol: the pitfalls of using tissue concentration data. *J Nucl Med* 1975; 16:248–249.
40. Kirschner AS, Ice RD. The author's reply [Letter]. *J Nucl Med* 1975; 16:248–249.
41. Loevinger R. Distributed radionuclide sources. In: Attix FH, Tochlin E, eds. Radiation dosimetry. 2nd ed. New York: Academic Press, 1969:51–88.
42. Feller PA. Internal dosimetry II. In: The physics of clinical nuclear medicine. AAPM Annual Summer School, Lexington: University of Kentucky, July 23–29, 1977:282–295.
43. Ortendahl DA, Hattner RS, Kaufman L, et al. A Bayesean algorithm for resolution recovery in clinical nuclear medicine. In: Deconick F, ed. Information processing in nuclear medicine. The Hague: Martinus Nijhoff, 1984:392.
44. Madsen MT, Park CP. Enhancement of SPECT images by fourier filtering the projection image set. *J Nucl Med* 1985; 26:395–402.